An Analysis of Bilge Keel Effects using RANS with Overset Grids Method

Motoki Araki[1], Kunihide Ohashi[1], Nobuyuki Hirata[1]

1. National Maritime Research Institute, Japan

Abstract: Roll damping effects due to bilge keels are one of the important topics for roll damping prediction. Since the mechanisms of the bilge keel effects are highly related to viscous phenomena, the roll decay with forward speed simulation of the US navy combatant DTMB5415 is conducted with URANS solver. Here the attached bilge keel is reproduced by using an overset grids method. The computed results show not quantitative but qualitative agreements with the experimental results. Moreover the CFD forced roll motion without bilge keels is simulated to analyze the bilge keel effects. From the comparison of the roll moment between these computed results, the model with bilge keels has larger roll rate component and smaller roll acceleration component than those of the model without bilge keel. The larger roll rate component could be caused by vortex shedding at the bilge keel tips and smaller roll acceleration component might be caused by interfering the accelerated flow around the body.

Key words: CFD, DTMB5415, roll decay,

1. Introduction

Bilge keel is one of the most basic and effective roll damping devices for ship stability. Since the roll damping is dominated by viscous effect and highly complex interactions with hull, bilge keels and free surface, potential flow simulations show some difficulties predicting roll damping on hull including bilge keels [1]. Therefore the semi-empirical roll damping prediction method is the most widely used for practical purpose e.g. Ikeda's method [2], which decomposes roll damping coefficients into various components. On the other hand, viscous computational fluid dynamics (CFD) has been developed and applied into dynamic ship motions such like Sakamoto et al. [3]. Moreover several URANS simulations have been done with overset girds method to reproduce the ship appendages including bilge keels e.g. Sadat-Hosseini et al. [4]. Therefore unsteady RANS (URANS) simulation could be one of the powerful tools to observe and predict the bilge keels effects on roll damping.

The first objective of this research is to validate the roll decay computed results using unstructured grid based URANS solver SURF [5] developed at NMRI

with an overset grids method. The second objective is to analyze the bilge keel effects on roll damping by observing the flow fields and roll moments during CFD roll decay and forced roll motion simulations with/without bilge keels.

2. Subject Ship

The US Navy combatant DTMB5415 (Fig. 1) famous as benchmarking ship is selected in this research. The roll decay test with forward speed in calm water was conducted in Iowa Institute of Hydraulic Research (IIHR) for the Gothenburg 2010 CFD Workshop [6]. The ship conditions of the roll decay simulations are shown in Table 1 which is same as the experimental conditions [7]. The bilge keels are conventional type with tapered ends.

Fig. 1   The US navy combatant DTMB5415

Table 1   Principal particulars

	Model scale
Scale ratio	46.6
Length between perpendiculars: L$_{PP}$ [m]	3.048
Breadth: B [m]	0.405
Draft: d [m]	0.132
Block coefficient: C$_B$	0.506
Metacentric height: GM [m]	0.043
Longitudinal position of center of gravity from F.P.: LCG [m]	1.536
Vertical position of center of gravity from waterline: VCG [m]	0.030
Roll radius of gyration: k$_{44}$=0.39B	0.158
Natural roll period: T$_\phi$ [s]	1.54
Bilge keel length: l$_{BK}$/L$_{PP}$	0.313
Bilge keel height at midship: b$_{BK}$/B	0.048

3. Computational Method

3.1   URANS Solver

The URANS solver SURF is applied in this research. The governing equations are continuity and incompressible URANS equations which are solved in the earth fixed coordinate system. A cell-centered finite volume method with unstructured grids is used for the spatial discritization. In this research all grids are constructed with hexahedral cells. The velocity-pressure coupling is accomplished with the artificial compressibility approach. The inviscid fluxes are evaluated by MUSCL typed 2nd-order upwinding scheme based on flux-difference-splitting of Roe [8], and the 2nd-order central differencing scheme is applied to the viscous fluxes. Following schemes are used for the time marching, the 2nd-order Euler backward differencing scheme for physical time step and 1st-order Euler backward differencing scheme for pseudo time step. More details on this solver can be found in the reference [5].

3.1   Overset Grids Method

An overset grid system UP_GRID [9] developed at NMRI is used as a pre-processor to generate overlapping assembly interconnecting each block. The basic algorithm of UP_GRID starts from searching in-wall cells located inside the solid surface of the other blocks by solving inverse problem in position space. Then the cells surrounding the in-wall cells are defined as receptor cells which receive flow information from the other cells. Moreover the outer boundaries of the each block are also set to be receptor cells to interconnect to the other blocks. After the receptor cells are settled, the non-in-wall and non-receptor cells vicinal to the other blocks' receptor cells are chosen to be donor cells which provide the flow information to the receptor cells. The cells of higher prioritized block are preferentially defined to be donor.

In this research 4 blocks in total (two bilge keel in starboard and port sides, bare hull, and background) are generated to express the model geometry. The highest priority is set to starboard sided bilge keel block, followed in order by port side bilge keel, bare hull, and background blocks. The details of the computational grids are given in Table 2 where 6.23M grid points are in total. The surface distributions and the slice of the midship section of the bilge keels, bare hull, and background blocks are shown in Fig. 2. Now the grid densities near the waterline are controlled to be higher than other parts for girth direction of the bare hull and the vertical direction of the background blocks are also controlled to resolve the wave elevation with single-phase level set method [10]. The minimum spacing of the solid walls are provided to be $y^+ < 1$ to resolve the boundary layer.

Figure 3 shows the grid assembly at the midship section. The upper figure shows the grid distribution before overset; the all blocks are overlapping together. The lower figure shows the non-in-wall and non-receptor cells after overset by UP_GRID. Comparing with the upper figure, the cells locating inside the solid surface and the outer boundary layers are removed while the outer boundary of the lowest

priority block, background block in this case, is maintained. Moreover the cells located in the region of the higher priority blocks are also removed.

Table 2   Grid sizes and decompositions

Block	i_m x j_m x k_m	Topology
Bilge keel Stb.	61x45x71 (0.19M)	H
Bilge keel Prt.	61x45x71 (0.19M)	H
Bare hull	141x157x81 (1.79M)	O-O
Background	249x161x101 (4.05M)	Cartesian
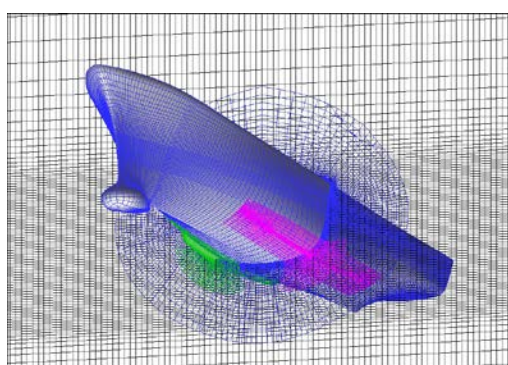
Fig. 2   Surface discretization and midship slice of the bilge keels, hull, and background blocks.
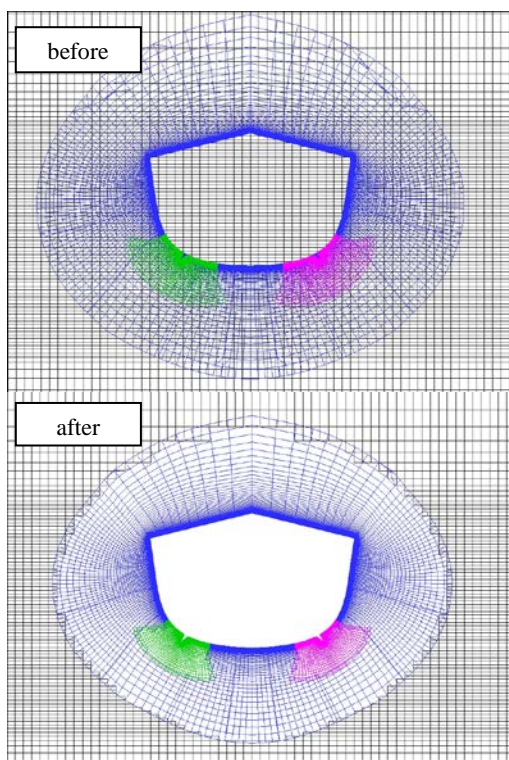
Fig. 3   UP_GRID overset grid assembly at midship section: before and after overset

4. Simulation Design

4.1   Test Case

The test conditions of the roll decay with forward speed simulations in calm water are shown in Table 3 same as the experimental condition [7] where U_c is constant towing speed and ϕ_0 is initial heel angle.

Table 3   Test condition

U_c [m/s]	Fr	Re [x10^6]	ϕ_0 [deg.]
0.754	0.138	2.56	-10.0

4.2   Grids and Simulation Design

The origin of the CFD coordinate system is at the intersection point of F.P., centerline, and undisturbed waterline. The x direction is from F.P. to A.P. and the y direction is the port to starboard, z direction is upward positive. Therefore it should be noted that the roll direction is reversed from the conventional ship stability coordinate.

The boundary conditions of the blocks are summarized in Fig. 4. The conditions of the solid walls are set to be no-slip conditions. In the background block, the upstream boundary is set to be inlet, the bottom, downstream, side boundaries are outlet and the top is far-field condition. Moreover wave damping zones are set at the outer boundaries of the background block to reduce the effects of the reflection wave. The distance from F.P. to upstream boundary of the background block is 1.5L_{PP}, 2.5L_{PP} from A.P. to downstream boundary, 1.5L_{PP} from centerline to side boundaries, and 1.5L_{PP} from waterline to bottom.

The simulation procedure is as follows: first the ship is towed with static heel angle (-10 degrees) for a while; and then the roll motion is released to start the roll decay simulation which is similar to the experimental procedure. Now 1 DOF roll motion is solved in this simulation; fixed trim and sinkage were given in the experiment. The dynamic roll motion is computed with moving grid method [3] as shown in Fig. 5. During the grid morphing, the region around the connect boundary between bare hull and background blocks are kept to maintain the initial overset information provided by UP_GRID.

In this case, the size of the physical time step and the position of the morphing area are important factors for the roll decay simulation. The large time step and the far morphing area from the center of rotation cause the large mesh motion and that could affect the interpolation of the level set function which creates numerical waves disturbing the roll motion [11]. Therefore the small time step and close morphing area are selected. Now the computation is performed with almost 380 time steps per the natural roll period.

The k-ω form of two-equation nonlinear explicit algebraic stress model (EASM) [12] is used for the turbulence model.
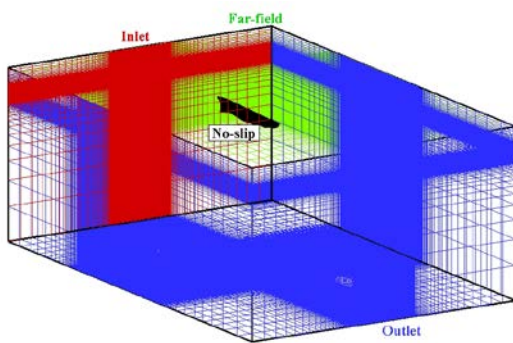

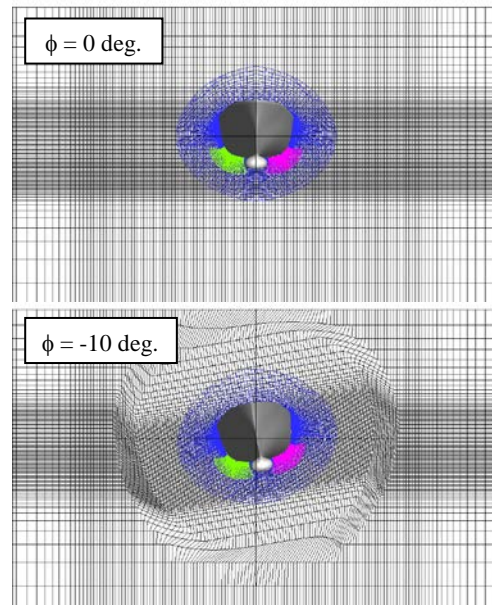
Fig. 4   Computational region and the boundary conditions

Fig. 5   Grid morphing by moving grid method at midship section (ϕ = 0 and -10 deg.).

5. Roll Decay Validation

5.1   Roll Motion and damping coefficients

The CFD roll decay simulation is executed according to the procedure of the previous section. Figure 6 shows the comparison of the EFD and CFD roll motion. The red circle symbol indicates the EFD result and the blue solid line shows the present CFD result. As shown in Fig. 6, the CFD result shows some agreements with the EFD. However the error of the roll amplitude and phase are increasing as time progress. Because the roll damping progress is one of the energy dissipation phenomena, the error is accumulating with the time progression. Therefore the small initial error could grow to the large error after a while.

The extinction coefficients *a, b, c* and equivalent linearized roll damping coefficients α_e are estimated from the time history of the roll motion based on the Baker's expression (Eqs. 1-3) [2].

$$\Delta\phi = a\phi'_n + b\phi'^2_n + c\phi'^3_n \qquad (1)$$

$$\alpha_e = \frac{\omega}{\pi}\left(a + b\phi_0 + c\phi_0^2\right) \qquad (2)$$

$$where \begin{cases} \Delta\phi = \phi_n - \phi_{n+1} \\ \phi'_n = (\phi_n + \phi_{n+1})/2. \end{cases} \qquad (3).$$

Here ϕ_n is the absolute values of the peak roll angles during the roll decay test and ω is the natural roll frequency. These coefficients are obtained with the first roll peak to the 11th peak (ϕ_1 to ϕ_{11}). The computed EFD and CFD extinction coefficients and the equivalent linearlized roll damping coefficient are shown in Table 4 and the extinction curves are shown in Fig. 7. As shown in Fig. 6 and the α_e values in Table 4, the CFD simulation overestimates the roll damping. Comparison of EFD and CFD flowfields could provide some guidelines for the better CFD results.
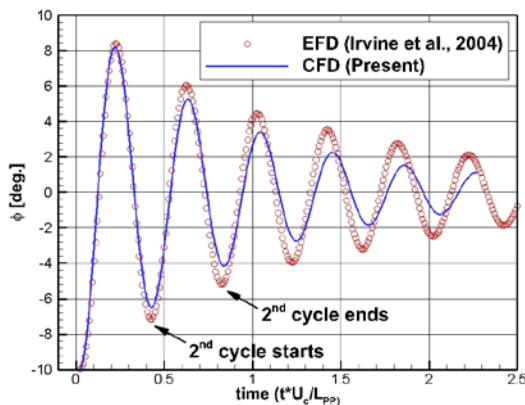

Fig. 6   Comparison of EFD and CFD roll motion during roll decay.

Table 4   EFD and CFD roll damping extinction coefficients and equivalent linearized coefficient

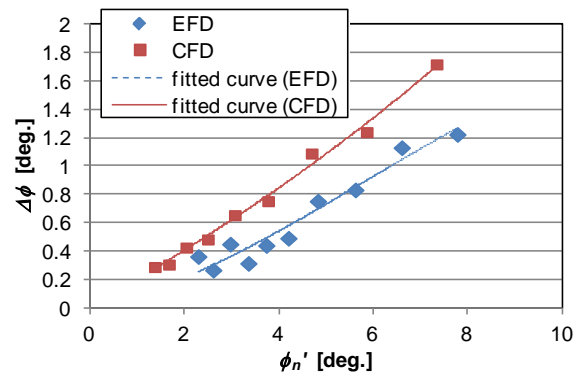|	EFD	CFD
a	0.06530	0.19413
b	0.02246	0.00296
c	-0.00128	0.00030
α_e	0.21026	0.32953

Fig. 7   Comparison of EFD and CFD extinction curves.

5.2   Flowfield

The EFD flowfield data during the roll decay was provided by Particle Image Velocimetry (PIV) measurements and servo wave probes (Irvine et al., 2004). Here Figs. 8-10 show the comparisons of EFD and CFD streamwise, horizontal, and vertical velocities (u, v, w) at x/L_{PP} = 0.675 section in vicinity of the port side bilge keel during the 2nd roll cycle. Now the 2nd roll cycle starts from the 2nd negative peak and ends at the 3rd negative peak as shown in Fig. 6. In Figs. 8-10, the velocity contours are shown when the roll angle reaches to the 1st negative peak (t/T_e=0/4), the 1st zerocross point (t/T_e=1/4), the positive peak (t/T_e=2/4), and the 2nd zerocross point (t/T_e=3/4) in the 2nd cycle.

Figure 8 shows distribution of the streamwise velocity at x/L_{PP} = 0.675. At the t/T_e=0/4, 1/4, 3/4, CFD results clearly show smaller low speed regions than the EFD which could indicate the strong numerical diffusion due to lack of the grid density near the bilge keels. On the other hand, the horizontal and vertical velocities in Figs. 9 and 10 show fairly good agreement with the EFD results similar to the other CFD results [6]. These results indicate the grid density in the streamwise direction could be not enough to resolve the vortex flow to the downstream. However, in total, CFD velocities seem to show qualitative agreements with the EFD results.

EFD and CFD wave elevations in the starboard side during the 2nd roll cycle are shown in Figs. 11 and 12. While the CFD results cannot simulate the wave propagation in far field, the trends of the variation of the wave elevation during the 2nd cycle in vicinity of the bow seem to be good agreement with the EFD results. Since the CFD fails to resolve the small waves in far field, the finer grid density might be required for all directions near the free surface. Moreover, since single O-O topology gird has difficulty clustering around the sonar dome, finer overset grid around the sonar dome might help simulating the vortex from the sonar dome.
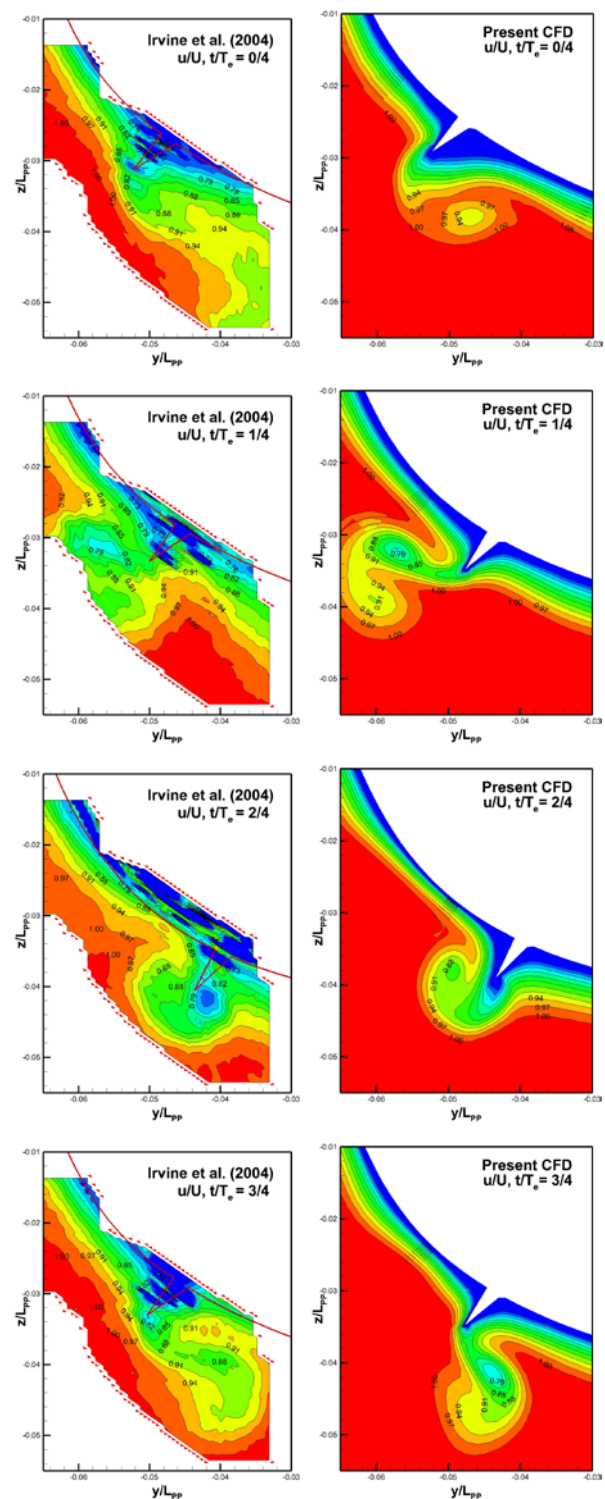

Fig. 8   Comparison of EFD and CFD streamwise velocity at $x/L_{PP}=0.675$ during the 2nd cycle of roll decay.
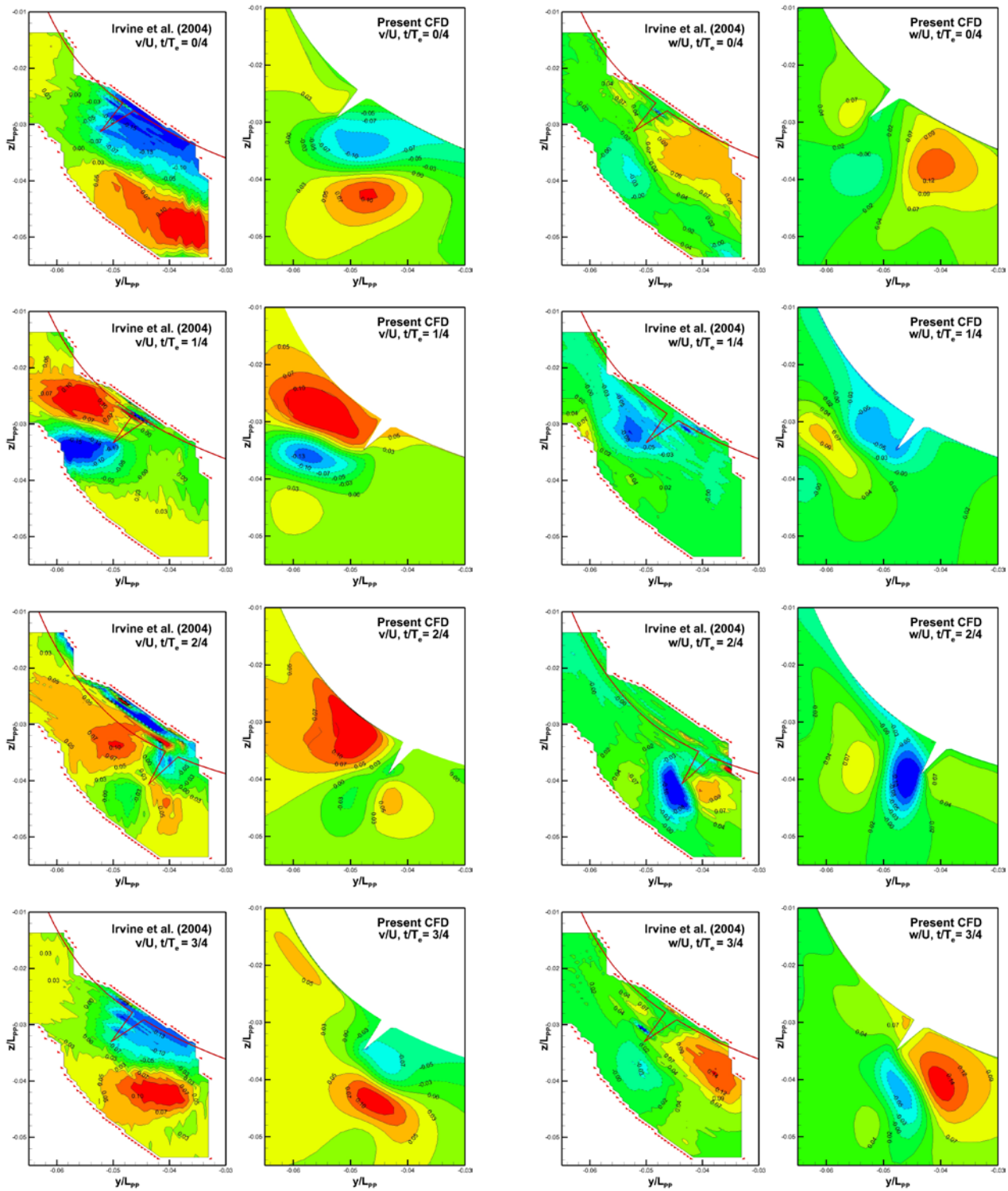
Fig. 9   Comparison of EFD and CFD horizontal velocity at x/L$_{PP}$=0.675 during the 2nd cycle of roll decay.

Fig. 10   Comparison of EFD and CFD vertical velocity at x/L$_{PP}$=0.675 during the 2nd cycle of roll decay.
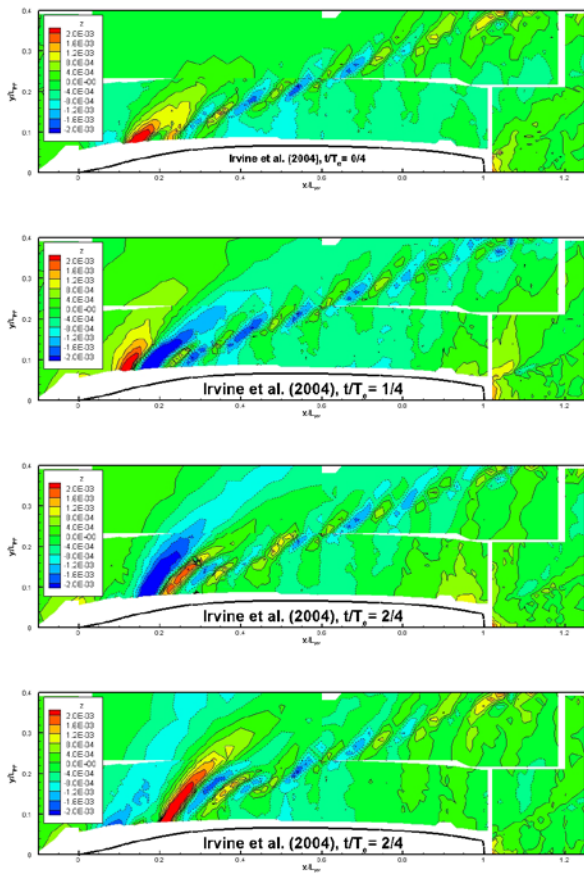
Fig. 11   Contours of the EFD wave elevation during the 2nd cycle of roll decay.
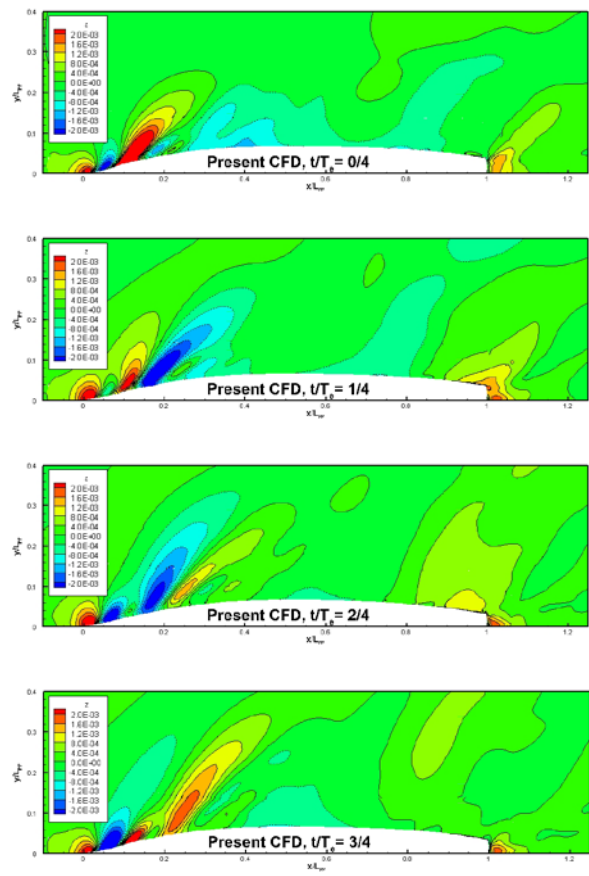

Fig. 12   Contours of the CFD wave elevation during the 2nd cycle of roll decay.

6. Bilge Keel Effects

6.1 Roll Decay and Forced Roll Motion without Bilge Keel

In this section, the bilge keel effects are evaluated by comparing the CFD roll decay and forced roll motion simulations with/without bilge keels. The previous CFD roll decay results are reused for the forced roll motion. Now the roll motion is forced to trace the CFD roll decay motion as shown in Fig. 6. Therefore the exactly same roll motion can be achieved in both cases with/without bilge keels.

The characteristics of the bilge keels could be demonstrated by comparing the roll moments, flowfield, and the pressure distribution on the hull surface with the same roll motion. Hereafter the roll decay simulations with/without bilge keels are termed RDwBK and RDwoBK, and the force roll motion without bilge keel is FRwoBK.

6.2 Comparison between RDw/woBK, and FRwoBK

Figure 13 shows the comparison of the roll moments at the CoG and roll angles between the RDw/woBK and FRwoBK. Now the roll moments are nondimensionalized with $0.5\rho U_c^2 L_{PP}^3$ and the hydrostatic restoring moments are extracted from the total roll moments and it is also assumed that the hydrostatic restoring moments of the RDw/woBK and FRwoBK are same. The RDwBK shows smaller roll angle than the RDwoBK due to the bilge keel effects. The roll moment of RDwBK has largest amplitude and the phase lag from the roll motion is very close to the 90 degrees which is identical for the roll damping. On the other hand, the moments of the RDwoBK and FRwoBK have smaller amplitude and the phase lag is larger than 90 degrees. The difference of the roll moment amplitudes between the RDwoBK and FRwoBK is caused by the slightly different roll rate between the two cases. Hereafter the comparison between RDwBK and FRwoBK is focused since the difference between the RDwoBK and FRwoBK is

small. In Fig. 14, the roll moments of RDwBK and FRwoBK are plotted with the roll rate and roll acceleration in the horizontal axis. Note that the initial transition parts are extracted in Fig. 14. In Fig. 14a, RDwBK shows larger negative incline than the FRwoBK which indicates the RDwBK has larger roll rate component. In Fig.14b, The FRwoBK spiral shows the larger positive incline than the RDwBK spiral which indicates the FRwoBK has larger roll acceleration component. Moreover the roll moments are separated to the roll rate and roll acceleration components as Eq. (4) using the least square method.

$$K' = \alpha\dot{\phi} + \beta\ddot{\phi} \qquad (4).$$

Here the α is roll rate component and the β is roll acceleration component. The separated results are shown in Table 5. As mentioned in Fig. 14, the RDwBK shows larger roll rate component and smaller acceleration component than those of FRwoBK.

The x axial vorticity (ω_x) at $x/L_{PP} = 0.675$ section during the 2nd roll cycle is shown in Figs. 15 and 16. Figure 16 shows the large vortices generated from the bilge keel tips while Fig. 15 merely shows very thin vortex layer on the body surface. In Fig. 16, large and strong vortices are generated at $t/T_e = 1/4$ and $3/4$ which is the zero crossing points of the roll angle synonymous with the peaks of the roll rate. Meanwhile relatively small vortices are generated at $t/T_e = 0/4$ and $2/4$ almost zero roll rate. From these results, the main component of the bilge keel roll damping related to the roll rate could be the eddy-making component as mentioned by Ikeda et al. [13].

The comparison of the RDwBK and FRwoBK pressure distribution at $x/L_{PP} = 0.675$ section during the 2nd roll cycle is shown in Fig. 17. The red solid line shows the pressure distribution of the RDwBK and the green line indicates that of the FDwoBK. The sharp pressure peaks can be found at the RDwBK's bilge keels positions in Fig.17. Even in far from the bilge keels, some discrepancies are shown between the RDwBK and FRwoBK pressure distribution which

could be the interaction effects between bilge keels and hull. Unexpectedly the larger pressure peak can be found at the zero roll rate points (t/Te = 0/4 and 2/4) than those of the points at the peaks of roll rate (t/Te = 1/4 and 3/4). Moreover the discrepancies between the RDwBK and FRwoBK are increasing along with increase of the roll acceleration which could cause the difference of the added moment of inertia. Going back to Fig. 13, the roll moment of the RDwBK is almost zero at roll angle peaks while the moments of FRwoBK and RDwoBK remains in restoring direction. These remaining moments could be one factor for the delay of the roll damping in the RDwoBK. At the roll peaks (t/T_e=0/4 and 2/4) in Fig. 17, the pressure at the bilge keels is acting to the direction cancelling the remaining moment. For example, focusing into the port side bilge keel at t/T_e=0/4 in Fig. 17, the pressure distribution of the RDwBK shows larger negative pressure than FRwoBK in the inner surface of the bilge keel and smaller negative pressure in the outer surface which generate the roll moment in opposite to the restoring direction. The bilge keel in starboard also shows similar pressure distribution with smaller magnitude. From these results, it could be presumed that the bilge keel might interfere the flow accelerated by the hull movement and that could make the roll acceleration component smaller than that of the no bilge keel case in stationary points.
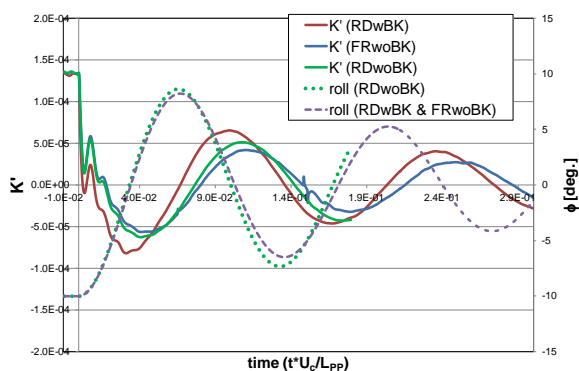

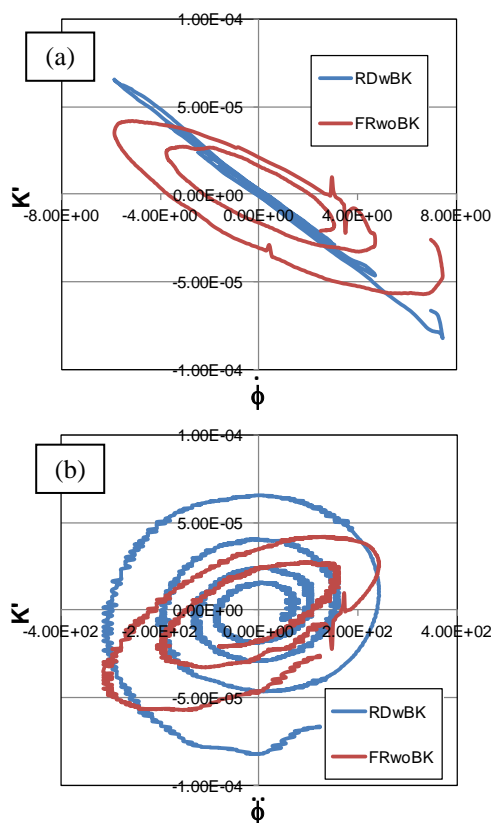**Fig. 14   Comparison of the RDwBK and FRwoBK roll moments with (a) roll rate, and (b) roll acceleration.**

Table 5   The comparison of the roll rate and roll acceleration components between RDwBK and FRwoBK

	RDwBK	FRwoBK
α [x 10^{-5}]	-1.05	-0.59
β [x 10^{-7}]	0.04	0.96

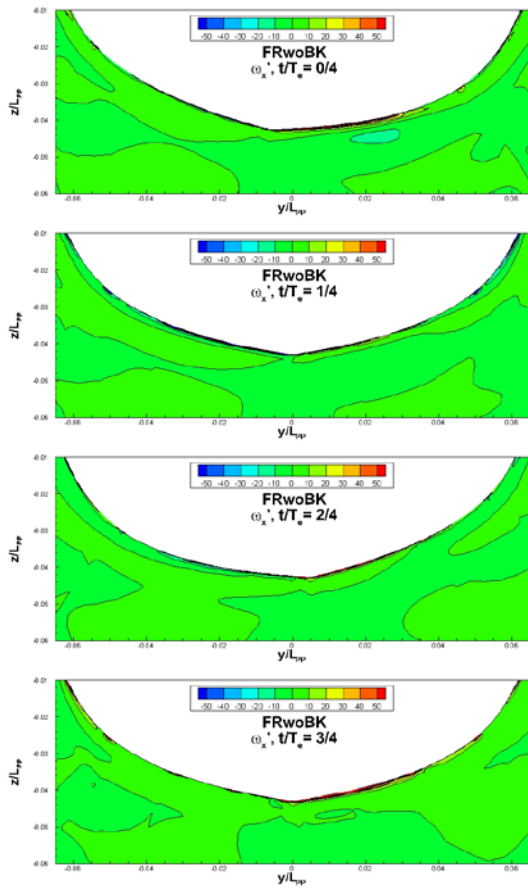**Fig. 13   Comparison of the RDwBK and FRwoBK roll moments.**

Fig. 15   Contours of the x axial vorticity (ω_x) at x/LPP = 0.675 section during the 2nd roll cycle in FRwoBK.
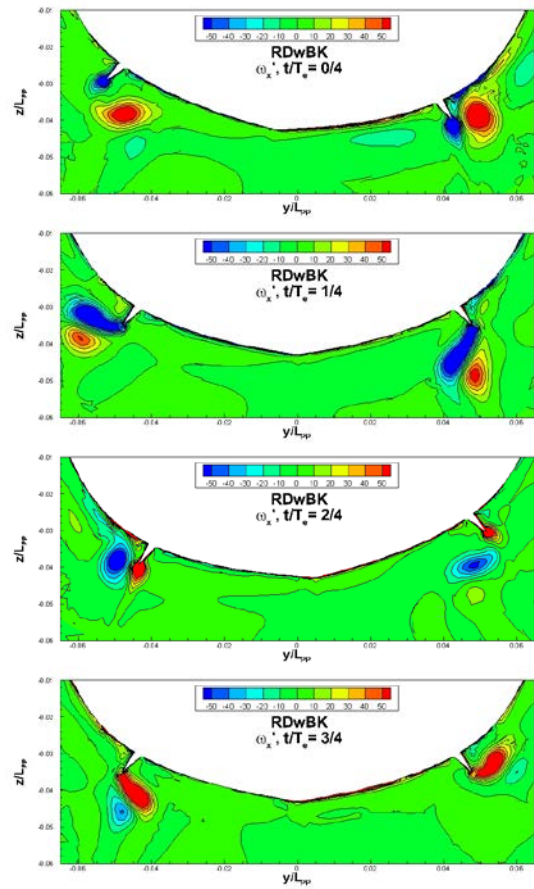
Fig. 16   Contours of the x axial vorticity (ω_x) at x/LPP = 0.675 section during the 2nd roll cycle in RDwBK.
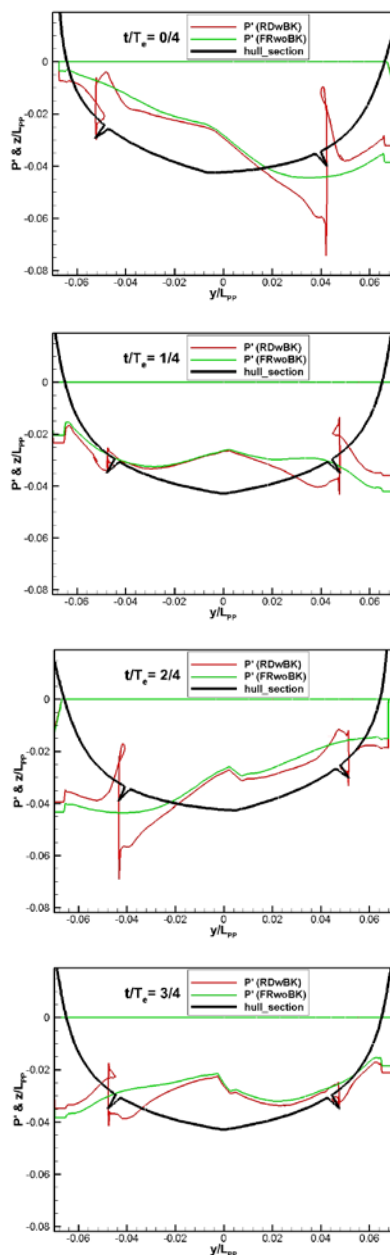
Fig. 17 Comparison of the RDwBK and FRwoBK pressure distribution at x/L$_{PP}$=0.675 during second cycle.

7. Conclusions

The CFD roll decay simulation using overset grids method is conducted with the US Navy combatant DTMB5415 installing bilge keels. The roll decay with forward speed simulation is validated with the experimental results. Moreover the CFD roll decay and forced roll motion simulation without bilge keels are

conducted to evaluate the bilge keel effects. By comparing these simulation results, the model with bilge keel shows larger roll rate component and smaller roll acceleration component than those of no bilge keel cases. The large vortex shedding from the bilge keel tips can be found at the roll rate peaks and the large difference of the pressure distribution at the bilge keel are shown in the roll acceleration peaks.

Acknowledgments

References

[1] Bassler, C., 2008, Roll Damping Mechanisms for a Wave-Piercing Tumblehome Hull Form, Proceeding of 6th Osaka Colloquium on Seakeeping and Stability of Ships.

[2] Himeno, Y., 1981, Prediction of Ship Roll Damping –State of the Art, Dept. of Naval Architecture and Marine Engineering, Univ. of Michigan, Report 239.

[3] Sakamoto, N., Ohashi, K., Kobayashi, H., Hirata, N., 2011, Analysis of non-linear/large-amplitude motions of submerged and floating bodies by URANS simulation with moving grid technique, Proceedings of 25th CFD Symposium, Osaka, Japan.

[4] Sadat-Hosseini, H., Carrica, P., Stern, F., Umeda, N., Hashimoto, H., Yamamura, S., Mastuda, A., 2011, CFD, system-based and EFD study of ship dynamic instability events: Surf-riding, periodic motion, and broaching, Ocean Engineering, Vol. 38, pp.88-110.

[5] Hino, T., 1997, A 3D unstructured grid method for incompressible viscous flows, Journal of the Society of Naval Architects of Japan, Vol. 183, pp. 9-15.

[6] Larsson, L., Stern, F., Visonneau, M., 2011, Numerical Ship Hydrodynamics, Proceedings of Gothenburg 2010 Workshop, December 8-10, Gothenburg, Sweden.

[7] Irvine, M., Longo, J., Sten, F., 2004, Towing-Tank Tests for Surface Combatant for Free Roll Decay and Coupled Pitch and Heave Motions, Proceedings of the 25th Symposium on Naval Hydrodynamics.

[8] Roe P.L., 1986, Characteristic-based scheme for the Euler equations, Annual Review of Fluid Mechanics, Vol. 18, pp. 337-365

[9]   Kodama, Y., Ohashi, K., Umezaki, Y., Hirata, N., 2012, Development of UP_GRID, and Overset Grid System for Computing Flows past Ship Hulls with Appendages, Proceedings of the 26th Computational Fluid Dynamics Symposium , Tokyo, Japan, D08-1.

[10] Hino, T., 1999, An interface capturing method for free surface flow computations of unstructured grids, Journal of the Society of Naval Architects of Japan, Vol. 186, pp. 177-183.

[11] Deng, G. B., Leroyer, A., Guilmineau, E., Queutey, P., Visonneau, M., Wackers, J., 2010, Verification and Validation for Unsteady Computation, Proceedings of Gothenburg 2010 Workshop on Numerical Ship Hydrodynamics, Vol. 2, pp. 447-452.

[12] Rumsey, L.C., Gatski, B.T., 2001, Recent Turbulence Model Advances Applied to Multielemet Airfoil Computations, Journal of Aircraft, Vol. 38, No. 5, pp. 904-910.

[13] Ikeda, Y., Himeno, Y., Tanaka, N., 1978, Components of Roll Damping of Ship at Forward Speed, Journal of Kansai Society of Naval Architects, No. 176, pp. 33-45.